

1 INTRODUCTION

2 Above Earth's atmosphere are the a pair of Van Allen radiation belts, a complex
3 and dynamic plasma environment that effects our technology-driven society. These
4 effects include: a higher radiation dose for astronauts and cosmonauts, higher chance
5 of spacecraft failure due to single event upsets that can lead to catastrophic latchups,
6 degradation of silicon (changing the silicon doping) from an extended radiation dose
7 that can degrade a transistor to the point where it no longer function as a switch,
8 and the degradation of the ozone layer due to the chemical production of NO_X and
9 HO_X molecules. With these effects in mind, it is no surprise that the radiation belts
10 have been extensively studied since their discovery in the 1960s.

11 One natural phenomenon in the radiation belts that has been a topic of interest
12 in the space physics community is wave-particle intersections that, as we will explore
13 throughout this dissertation, can accelerate particles to very high energies (e.g. \approx
14 MeV for electrons) and scatter them into the atmosphere.

15 The goal of this dissertation is to study the wave-particle mechanism that
16 scatters microbursts, a sub-second impulse of electrons into Earth's atmosphere.
17 Before we dive deep into the physics of wave-particle interactions, an introduction to
18 Earth's magnetosphere is warranted. Single charged particle motion in Earth's electric
19 and magnetic fields will be described first. Then the major particle populations in
20 the magnetosphere and the coupling between them will be described. Lastly, a brief
21 overview of wave-particle interactions and their effects will be presented.

22 Charged Particle Motion in Electric and Magnetic Fields

A charged particle trapped in the magnetosphere will experience three types
of periodic motion in Earth's nearly dipolar magnetic field. The three motions are

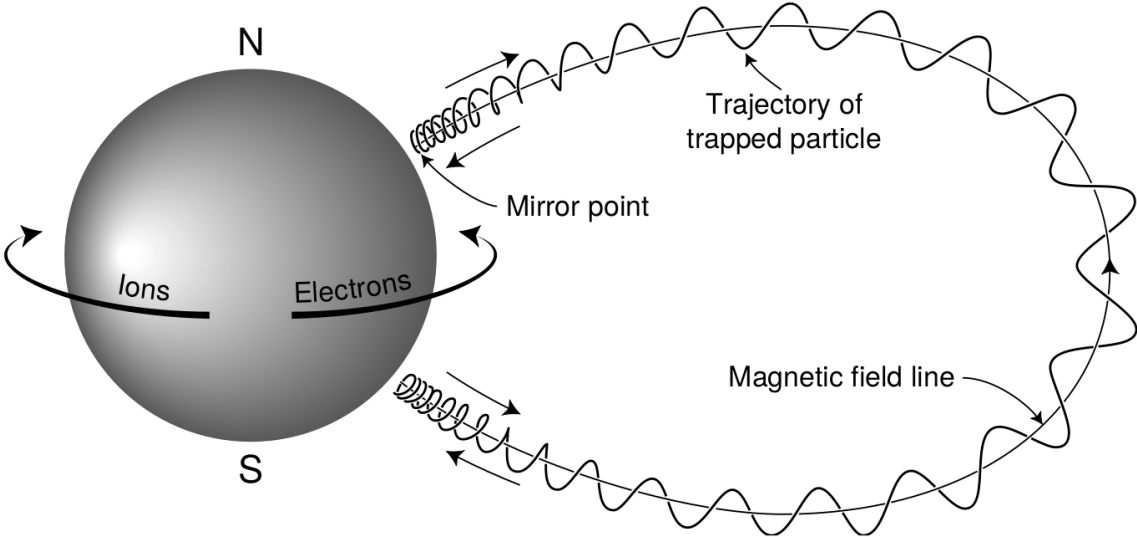


Figure 1.1: The three periodic motions of charged particles in Earth's dipole magnetic field. These motions are: gyration about the magnetic field line, bounce motion between the magnetic poles, and azimuthal drift around the Earth. Figure from (Baumjohann and Treumann, 1997).

ultimately due to the Lorentz force that a particle of momentum \vec{p} , charge q , and velocity \vec{v} experiences in an electric field \vec{E} and magnetic field \vec{B} and is given by

$$\frac{d\vec{p}}{dt} = q(\vec{E} + \vec{v} \times \vec{B}). \quad (1.1)$$

- ²³ In the magnetosphere, the three periodic motions in decreasing frequency are gyration,
- ²⁴ bounce, and drift and are schematically shown in Fig. 1.1. Each of periodic these
- ²⁵ motions have a corresponding conserved quantity i.e. an adiabatic invariant.

The highest frequency periodic motion is gyration about a magnetic field of magnitude B . This motion is circular with a Larmor radius of

$$r = \frac{mv_{\perp}}{|q|B} \quad (1.2)$$

where m is the mass and v_{\perp} the particle's velocity perpendicular to \vec{B} . This motion

has a corresponding gyrofrequency

$$\Omega = \frac{|q|B}{m} \quad (1.3)$$

in units of radians/second. Inside the radiation belts the electron gyrofrequency, Ω_e is on the order of a kHz. The corresponding adiabatic invariant is found by integrating the particle's canonical momentum around the particle's path of gyration

$$J_i = \oint (\vec{p} + q\vec{A}) \cdot d\vec{l} \quad (1.4)$$

where J_i is the i^{th} adiabatic invariant and \vec{A} is the magnetic vector potential. This integral is carried out by integrating the first term over the circumference of the gyro orbit and integrating the second term using Stokes theorem to calculate the magnetic flux enclosed by the gyro orbit. With suitable integration, $J_1 \sim v_\perp^2/B$ and is conserved as the frequency of the driving force, ω satisfies $\omega \ll \Omega_e$.

The second highest frequency periodic motion is bouncing due to a parallel gradient in \vec{B} . This periodic motion naturally arises in the magnetosphere because Earth's magnetic field is stronger near the poles, and artificially in the laboratory in magnetic bottle machines. To understand this motion we first need to define the concept of pitch angle α as the angle between \vec{B} and \vec{v} which is schematically shown in Fig. 1.2a. The pitch angle relates v with v_\perp , and $v_{||}$ (the component of the particles velocity parallel to \vec{B}). As shown in 1.2b and c, a larger α will tighten the particle's helical trajectory and vice versa.

Assuming the particle's kinetic energy is concerned, the conservation of J_1 implies that given a particle's $v_\perp(0)$ and $B(0)$ at the magnetic equator (where Earth's magnetic field is usually at a minimum), we can calculate its $v_\perp(s)$ along the particle's path s by calculating $B(s)$ from magnetic field models. The particle's perpendicular

velocity is then related via

$$\frac{v_{\perp}^2(0)}{B(0)} = \frac{v_{\perp}^2(s)}{B(s)} \quad (1.5)$$

³⁹ which can be rewritten as

$$\frac{v^2 \sin^2 \alpha(0)}{B(0)} = \frac{v^2 - v_{\parallel}^2(s)}{B(s)} \quad (1.6)$$

⁴⁰ and re-arranged to solve for $v_{\parallel}(s)$

$$v_{\parallel}(s) = v \sqrt{1 - \frac{B(s)}{B(0)} \sin^2 \alpha(0)} \quad (1.7)$$

⁴¹ which will tend towards 0 when the second term in the radical approaches 1.

⁴² The location where $v_{\parallel}(s) = 0$ is called the mirror point and is where a particle
⁴³ stops and reverses direction. Since Earth's magnetic field is stronger towards the
⁴⁴ poles, the mirroring particle will execute periodic bounce motion between its two
⁴⁵ mirror points in the northern and southern hemispheres. The corresponding adiabatic
⁴⁶ invariant, J_2 is

$$J_2 = \oint p_{\parallel} ds \quad (1.8)$$

where ds describes the particle path between the mirror points in the northern and southern hemispheres (see Fig. 1.1). J_2 is found by substituting Eq. 1.7 into Eq. 1.8 and defining the magnetic field strength at the mirror points as B_m where $\alpha(m) = 90^\circ$.

The J_2 integral can be written as

$$J_2 = 2p \int_{m_n}^{m_s} \sqrt{1 - \frac{B(s)}{B(m)}} ds \quad (1.9)$$

⁴⁷ where m_n and m_s are the northern and southern mirror points, respectively. The

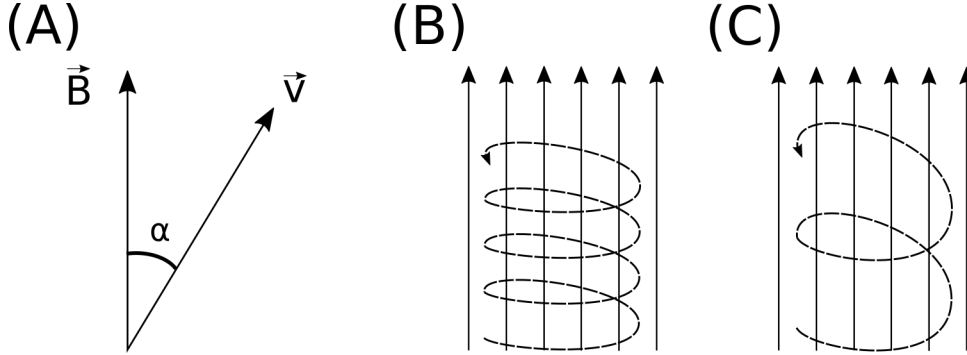


Figure 1.2: Charged particle motion in a uniform magnetic field \vec{B} . Panel (A) shows the geometry defining the pitch angle, α . Panel (B) and (C) show two helical electron trajectories with dashed lines assuming a large and small α (corresponding to a small and large parallel velocity $v_{||}$), respectively.

⁴⁸ bounce period can be estimated (e.g. Baumjohann and Treumann, 1997) to be

$$t_b \approx \frac{LR_e}{\sqrt{W/m}}(3.7 - 1.6 \sin \alpha(0)) \quad (1.10)$$

⁴⁹ where L is the L -shell which describes the distance from the Earth's center to the
⁵⁰ location where a particular magnetic field line crosses the magnetic equator, in units
⁵¹ of Earth radii, R_e . W is the particle's kinetic energy. As with gyration, a particle
⁵² bounces as long as $\omega \ll \Omega_b$, where Ω_b is the bounce frequency.

⁵³ At this stage it is instructional to introduce the notion of the loss cone pitch
⁵⁴ angle, α_L . A particle with $\alpha \leq \alpha_L$ will mirror at or below ≈ 100 km altitude in the
⁵⁵ atmosphere. A particle at those altitudes will encounter Earth's atmosphere and has
⁵⁶ a significant probability of Coulomb scattering with atmospheric particles and be lost
⁵⁷ to the atmosphere.

⁵⁸ The slowest periodic motion experienced by charged particles in Earth's mag-
⁵⁹ netic field is azimuthal drift around the Earth. This drift results from a combination of
⁶⁰ a radial gradient in \vec{B} and the curvature of the magnetic field. The radial gradient drift
⁶¹ arises because Earth's magnetic field is stronger near the Earth where the particle's

62 gyroradius radius of curvature is smaller as it gyrates towards stronger magnetic field,
 63 and larger when it gyrates outward. The overall effect is the particle gyro orbit does
 64 not close on itself and negatively charged particles drift East and positively charged
 65 particles drift West. The radial gradient drift is enhanced by the centrifugal force that
 66 a particle experiences as it bounces along the curved field lines. The drift adiabatic
 67 invariant, J_3 is found by integrating Eq. 1.4 over the complete particle orbit around
 68 the Earth. The shape of this drift orbit is otherwise known as a drift shell. For J_3 ,
 69 the first term is negligible and the second term is the magnetic flux enclosed by the
 70 drift shell, Φ_m i.e. $J_3 \sim \Phi_m$.

71 Figure 1.3 from Schulz and Lanzerotti (1974) shows contours of the gyration,
 72 bounce, and drift frequencies for electrons and protons in Earth's dipole magnetic
 73 field.

Up until now we have considered the three periodic motions due Earth's magnetic field and the absence of electric fields. If \vec{E} is present, a particle's center of gyration i.e., averaged position of the particle over a gyration, will drift with a velocity perpendicular to both \vec{E} and \vec{B} . The drift velocity can be solved directly from Eq. 1.1 and is

$$\vec{v}_E = \frac{\vec{E} \times \vec{B}}{B^2}. \quad (1.11)$$

74 Lastly, for more detailed derivations of these motions, see the following texts:
 75 Baumjohann and Treumann (1997); Schulz and Lanzerotti (1974); Tsurutani and
 76 Lakhina (1997).

77 Particle Populations and Their Interractions in the Magnetosphere

78 The single-particle motion in Earth's magnetic field described in the previous
 79 section is a prerequisite to understanding how magnetospheric particles organize into

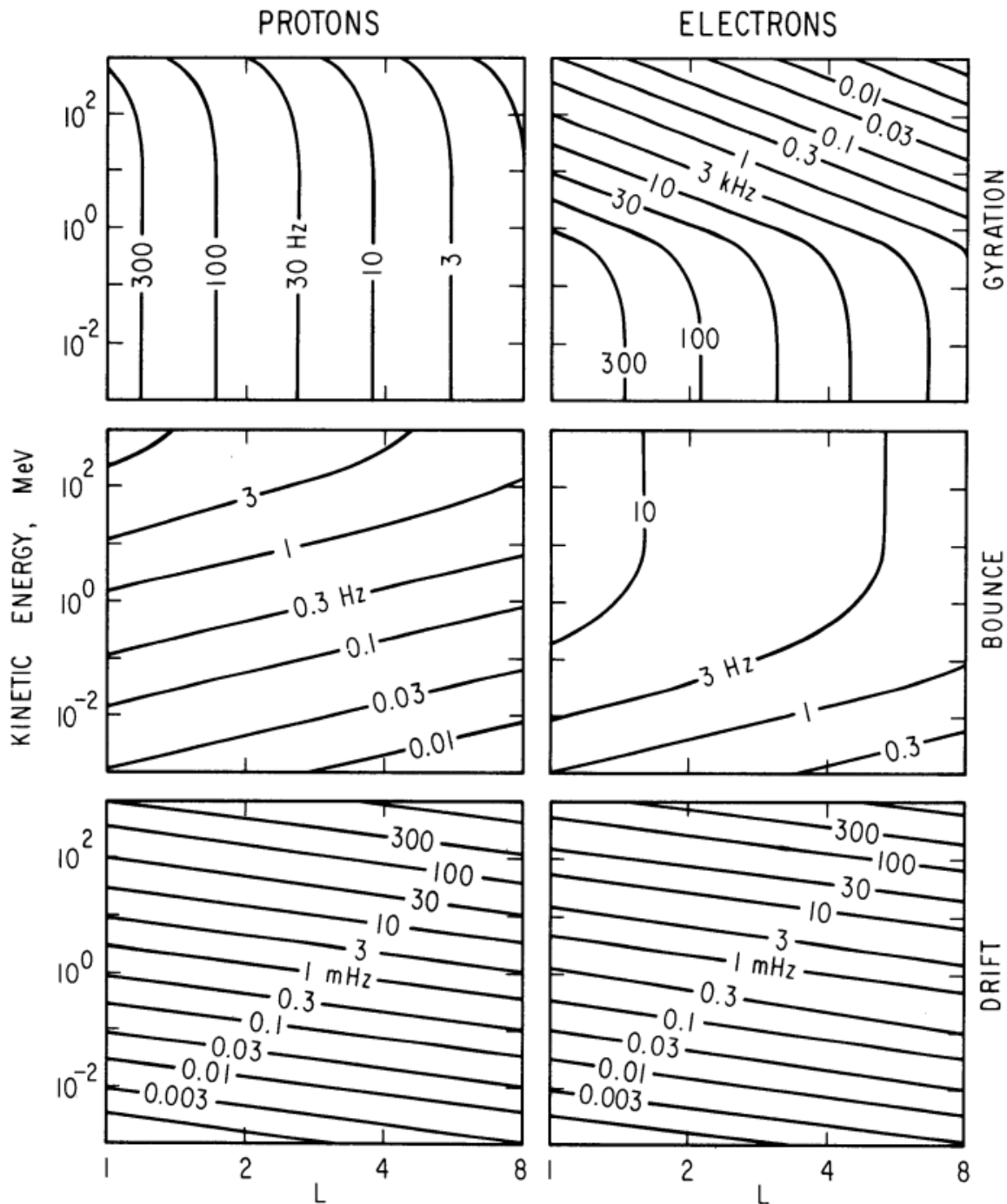


Figure 1.3: Contours of constant gyration, bounce, and drift frequencies for electrons and protons in a dipole field. Figure from Schulz and Lanzerotti (1974).

macroscopic populations. The structure of the outer magnetosphere is shown in Fig. 1.4 and inner magnetosphere in Fig. 1.5. In this section we will introduce the various particle populations in the magnetosphere and how they couple.

The sun and its solar wind are ultimately the source of energy input into the magnetosphere. The solar wind at Earth's orbit is a plasma traveling at supersonic speeds with an embedded interplanetary magnetic field (IMF). When the solar wind encounters Earth's magnetic field the plasma can not easily penetrate into the magnetosphere, rather it drapes around the magnetosphere forming a cavity in the solar wind that is roughly shaped as shown in Fig. 1.4. Because the solar wind is supersonic at 1 AU, a bow shock exists upstream of the magnetosphere. The solar wind plasma, after it is shocked by the bow shock, flows around the magnetosphere inside the magnetosheath. The surface where the solar wind ram pressure and Earth's magnetic pressure balance is termed the magnetopause, which can be thought of as a boundary between the solar wind's and Earth's plasma environments. This is a slightly naive description of the magnetopause, but is nonetheless an instructive conceptual picture. The shocked plasma then flows past the Earth where it shapes the magnetotail. In the magnetotail the solar wind magnetic pressure balances Earth's magnetic field pressure in the lobes. The magnetotail extends on the order of 100 R_E downstream of Earth [Add citation](#), and the tailward stretching of magnetic field lines creates the plasma sheet which exists in the region of low magnetic field strength near the magnetic equator [Add citation](#). The plasma sheet flows from dusk to dawn (out of the page in Figs. 1.4 and 1.5) and this current is connected to a zoo of other currents in the magnetosphere which is beyond the scope of this dissertation.

The idea of the magnetopause as a barrier between the solar wind and the magnetosphere is not entirely accurate due to the presence of reconnection. Reconnection was first conceived by Dungey (1961) who described the convection of

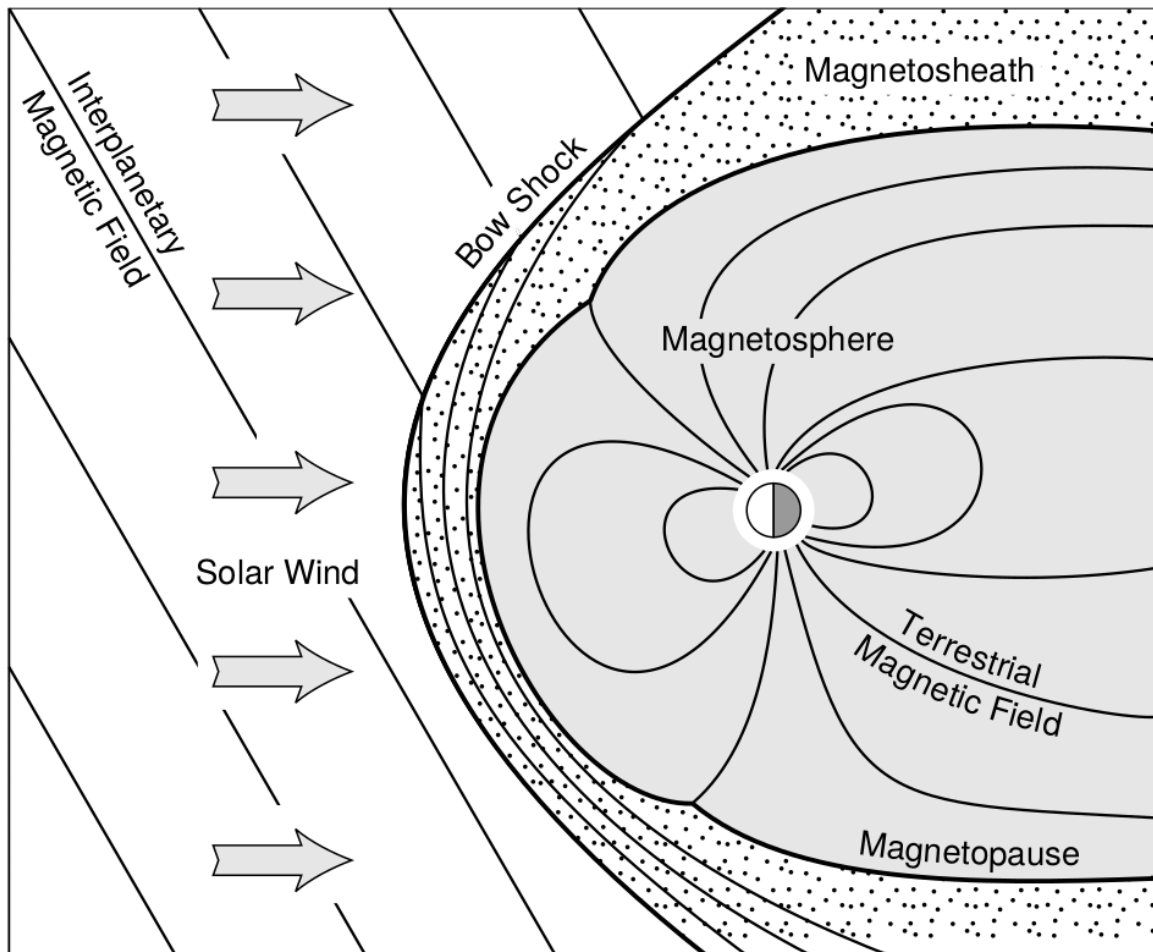


Figure 1.4: Macroscopic structures in the outer magnetosphere. The solar wind with its frozen-in interplanetary magnetic field is shown on the left and is traveling supersonically towards the right. The solar wind envelops Earth's magnetic field to create the magnetosphere cavity. Since the solar wind is traveling supersonically, it creates a bow shock up stream. Downstream of the bow shock the shocked solar wind plasma inside the magnetosheath flows around the magnetopause, a boundary between the solar wind and magnetosphere. Figure from Baumjohann and Treumann (1997).

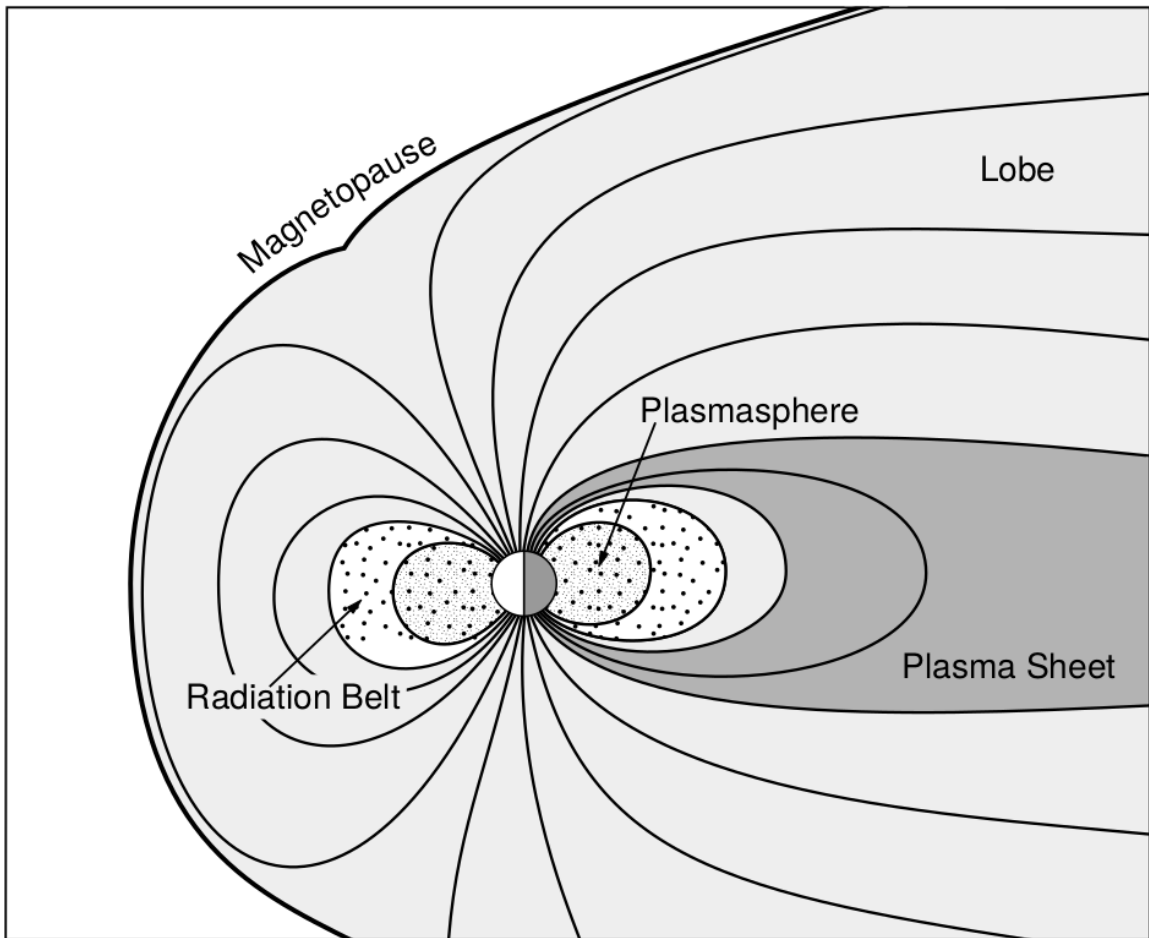


Figure 1.5: Macroscopic structures in the inner magnetosphere most relevant to this dissertation. The plasmasphere, and the radiation belts are shown and ring current is co-located there as well. Sun is to the left. Figure from Baumjohann and Treumann (1997).

106 Earth's magnetic field between the bow and tail regions of the magnetosphere. This
 107 process is known as the Dungey cycle and is most effective when the IMF is pointing
 108 southward as is shown in Fig. 1.6 part 1. As the IMF contacts Earth's magnetic
 109 field it reconnects with it so that Earth's magnetic field is directly connected to the
 110 IMF. Then as the solar wind flows tailward the IMF drags Earth's magnetic field
 111 towards the magnetotail as shown in Fig. 1.6 parts 2-6. As more and more magnetic
 112 field lines are draped in the magnetotail, magnetic pressure increases in the lobes
 113 which squeezes the plasma sheet until Earth's magnetic field reconnects as is shown
 114 in Fig. 1.6 part 7. Lastly, Fig. 1.6 part 8 shows the newly merged magnetic field
 115 line and the plasma frozen on it moves Earthward under the magnetic tension force
 116 to become more dipolar. This is called a dipolarization of the magnetic field, and the
 117 plasma frozen on these field lines can be observed as injections (e.g. Turner et al.,
 118 2015). Injection of plasma into the inner magnetosphere is one of the drivers of inner
 119 magnetosphere dynamics. **Should I talk about the K-H instability and how there**
 120 **could be micro reconnection? i.e. cite a paper or two that support or refute that**
 121 **idea.**

122 Inner Magnetosphere Populations

123 Before we describe the inner magnetosphere particle populations, we first need to
 124 describe the coordinate system used to organize the inner magnetosphere populations.
 125 The first coordinate was defined in section 1 and is the L shell. L shell can be thought
 126 of as an analogue to a radius but in a dipole geometry. The azimuthal coordinate
 127 is the magnetic local time (MLT). For an observer above Earth's north pole looking
 128 down, MLT is defined to be 0 (midnight) in the anti-sunward direction, and increases
 129 in the counter-clockwise direction with 6 at dawn, 12 at noon (sunward direction),
 130 and 18 in dusk. The last coordinate used in this dissertation is the magnetic latitude,

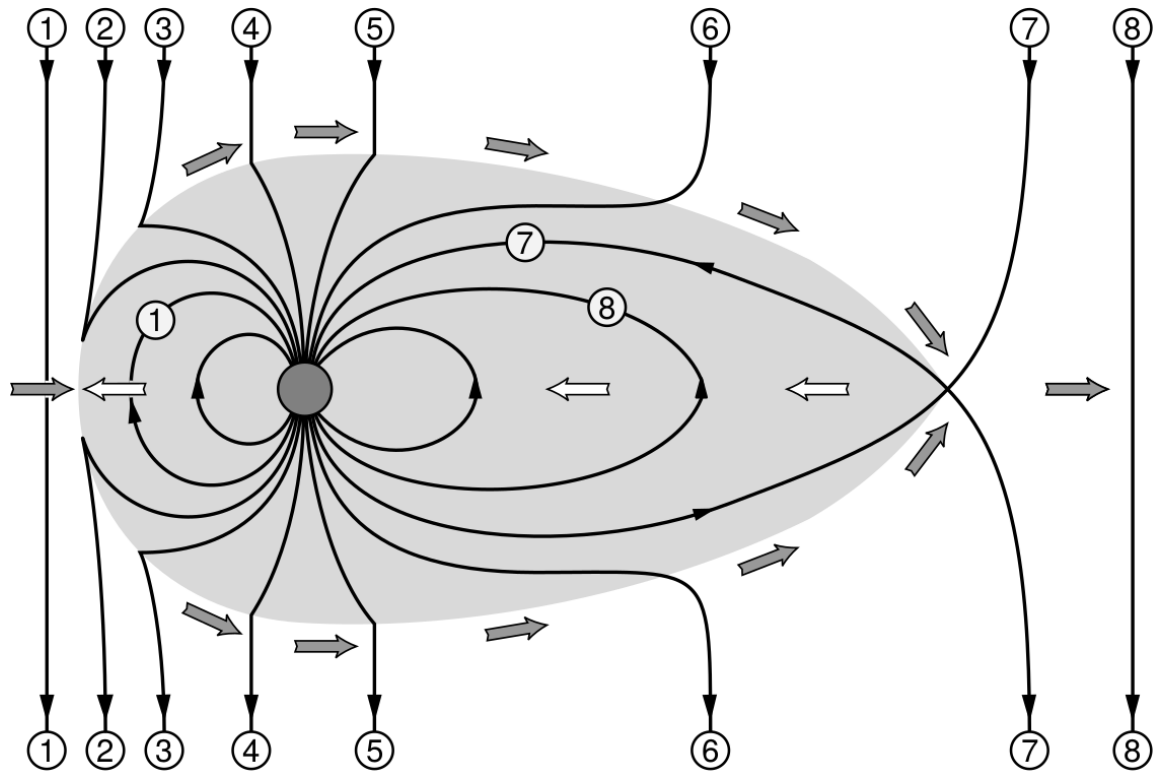


Figure 1.6: The series of steps involved in magnetic reconnection with a southward IMF. Figure from Baumjohann and Treumann (1997).

₁₃₁ λ which is analogous to the latitude coordinate and is defined to be 0 at the magnetic
₁₃₂ equator.

₁₃₃ The low energy particle dynamics in the inner magnetosphere are organized by
₁₃₄ two electric fields: the co-rotation and the dawn-dusk electric fields. The co-rotation
₁₃₅ electric field arises from the rotation of Earth's magnetic field. Since particles are
₁₃₆ frozen on magnetic field lines and the plasma conductivity is effectively infinite, to
₁₃₇ a non-rotating observer, Earth's rotation appears as a radial electric field that drops
₁₃₈ off as $\sim L^2$. This electric field makes particles orbit around the Earth due to the
₁₃₉ $\vec{E} \times \vec{B}$ drift. The other electric field, pointing from dawn to dusk is called the
₁₄₀ convection electric field and is formed by the Earthward transport of particles from
₁₄₁ the magnetotail that appears as an electric field to a stationary observer (with respect
₁₄₂ to Earth). The superposition of the co-rotation and convection electric fields
₁₄₃ results in a potential field shown in Fig. 1.7. The shaded area in Fig. 1.7 shows
₁₄₄ the orbits on which low energy electrons are trapped, and outside are the untrapped
₁₄₅ particles. The dynamic topology of the shaded region in Fig. 1.7 is controlled by only
₁₄₆ the convection electric field which is dependent on the solar wind speed and the IMF.
₁₄₇ The lowest energy particles, that are most effected by these electric fields, make up
₁₄₈ the plasmasphere.

₁₄₉ Plasmasphere The plasmasphere is a dense ($n_e \sim 10^3/\text{cm}^3$), cool plasma
₁₅₀ ($\sim \text{eV}$) that extends to $L \sim 4$ (extent is highly dependent on the solar wind and
₁₅₁ magnetospheric conditions) and is sourced from the ionosphere. The two main
₁₅₂ mechanisms that source the cold plasma from the ionosphere are ultraviolet ionization
₁₅₃ by sunlight and particle precipitation. The ultraviolet ionization by sunlight is
₁₅₄ strongly dependent on the time of day (day vs night), latitude (more ionization near
₁₅₅ the equator). The ionization due to particle precipitation, on the other hand, is highly

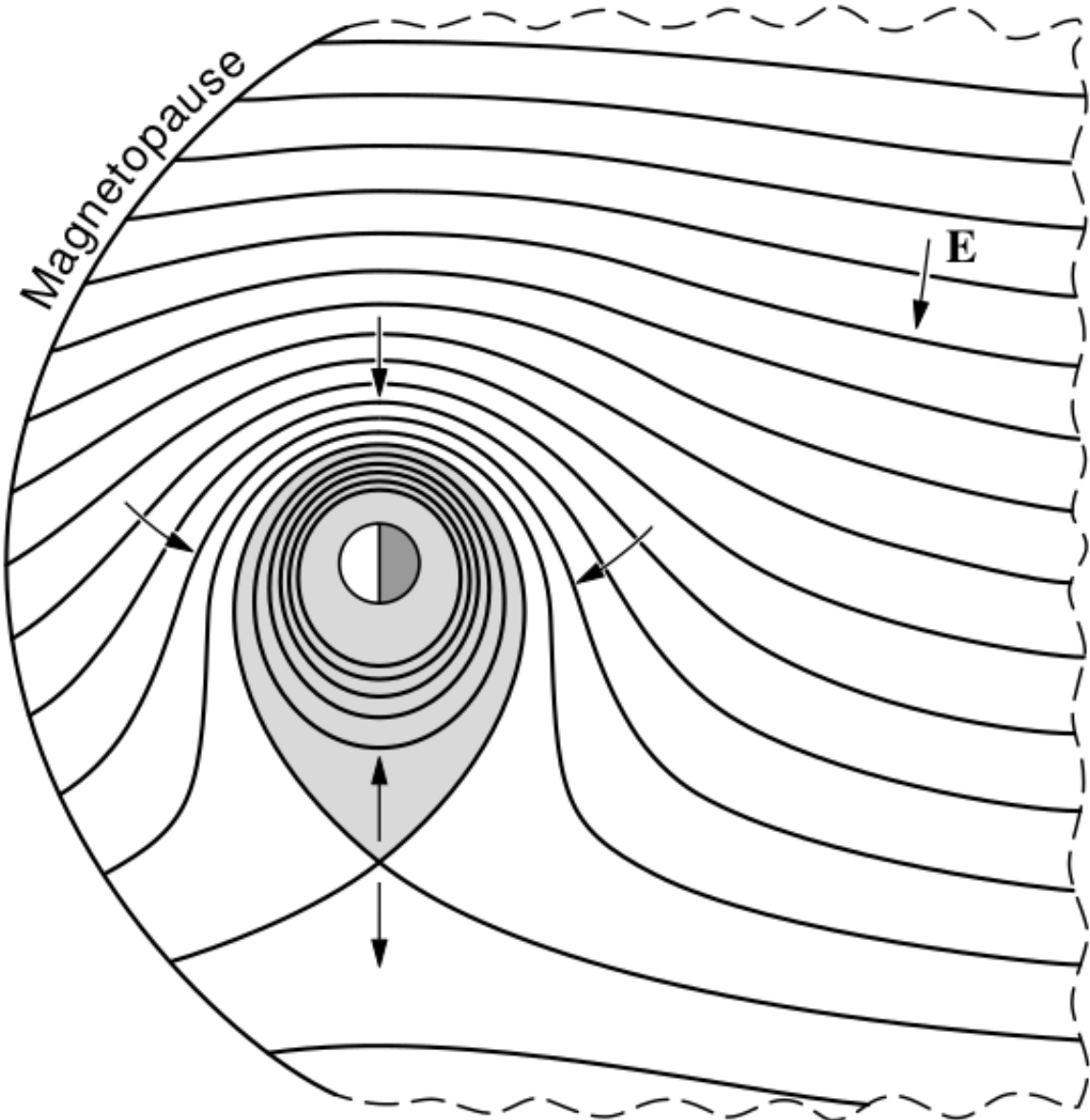


Figure 1.7: Equipotential lines and electric field arrows due to the superposition of the co-rotation and convection electric fields. Electrons in the shaded region execute closed orbits. Outside of the shaded regions the electrons are not trapped and will escape. The region separating the two regimes is called the Alfvén layer. Figure from Baumjohann and Treumann (1997).

¹⁵⁶ dependent on magnetospheric conditions, and mostly occurs at high latitudes.

¹⁵⁷ The outer boundary of the plasmasphere is the plasmapause which is typically
¹⁵⁸ identified as a steep radial gradient in plasma density from $\sim 10^3/\text{cm}^3$ to $\sim 1/\text{cm}^3$. As
¹⁵⁹ we will see throughout this dissertation, the location of the plasmapause is important
¹⁶⁰ to model (e.g. O'Brien and Moldwin, 2003) and understand since the plasma density
¹⁶¹ strongly controls the efficiency of particle scattering (Horne et al., 2005).

¹⁶² Ring Current The next higher energy population is the ring current. This
¹⁶³ population consists of protons and electrons between tens and a few hundred keV
¹⁶⁴ that drift around the Earth. The orbits of higher energy particles are not as effected
¹⁶⁵ by the convection and co-rotation electric field, rather they drift around the Earth
¹⁶⁶ due to gradient and curvature drifts. Since the direction of the drift is dependent on
¹⁶⁷ charge, protons drift west around the Earth and electrons drift East. This has the
¹⁶⁸ effect of creating a current around the Earth.

¹⁶⁹ The ring current generates a magnetic field which decreases the magnetic field
¹⁷⁰ strength on Earth's surface and increases it outside of the ring current. The decrease
¹⁷¹ of Earth's magnetic field strength is readily observed by a system of ground-based
¹⁷² magnetometers and is merged into a Disturbance Storm Time (DST) index. An
¹⁷³ example of a DST index time series from a coronal mass ejection (CME) driven 2015
¹⁷⁴ St. Patrick's Day storm is shown in Fig. 1.8. The ring current is sometimes first
¹⁷⁵ depleted and DST increases slightly (initial phase or sudden storm commencement).
¹⁷⁶ Then the ring current is rapidly built up during which DST rapidly decreases (main
¹⁷⁷ phase). Lastly the ring current gradually decays toward its equilibrium state over a
¹⁷⁸ period of a few days and DST increases towards 0 (recovery phase). The DST index
¹⁷⁹ along with other indicies are readily used by the space physics community to quantify
¹⁸⁰ the global state of the magnetosphere.

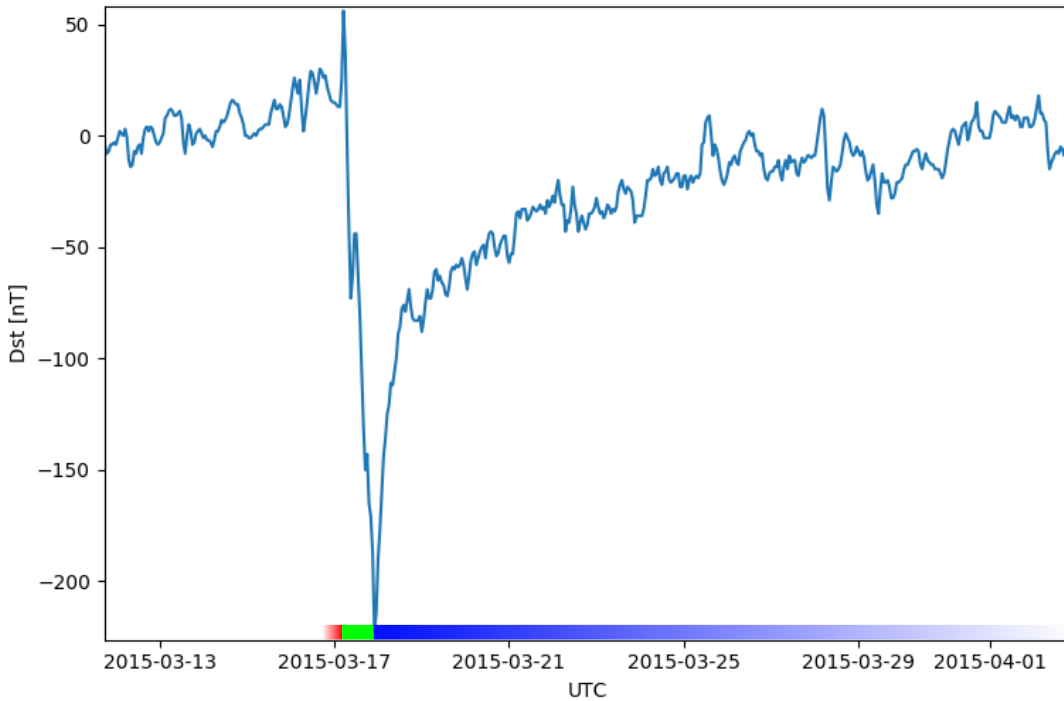


Figure 1.8: The DST index during the St. Patrick's Day 2015 storm. This storm was caused by a coronal mass ejection on March 15th, 2015. The storm phases are: initial phase, main phase, and recovery phase. The initial phase occurred when the Dst peaked at +50 nT on March 17th during which the ring current was eroded by the coronal mass ejection during the interval shown by the red bar. Then the rapid decrease to ≈ -200 nT was during the main phase where many injections from the magnetotail pumped up the ring current which reduced Earth's magnetic field strength at the ground and is shown with the green bar. Lastly, the recovery phase lasted from March 18th to approximately March 29th during which the ring current particles were lost and the ring current returned to its equilibrium state. The recovery phase is shown with the blue bar.

The Earth's Electron Radiation Belts

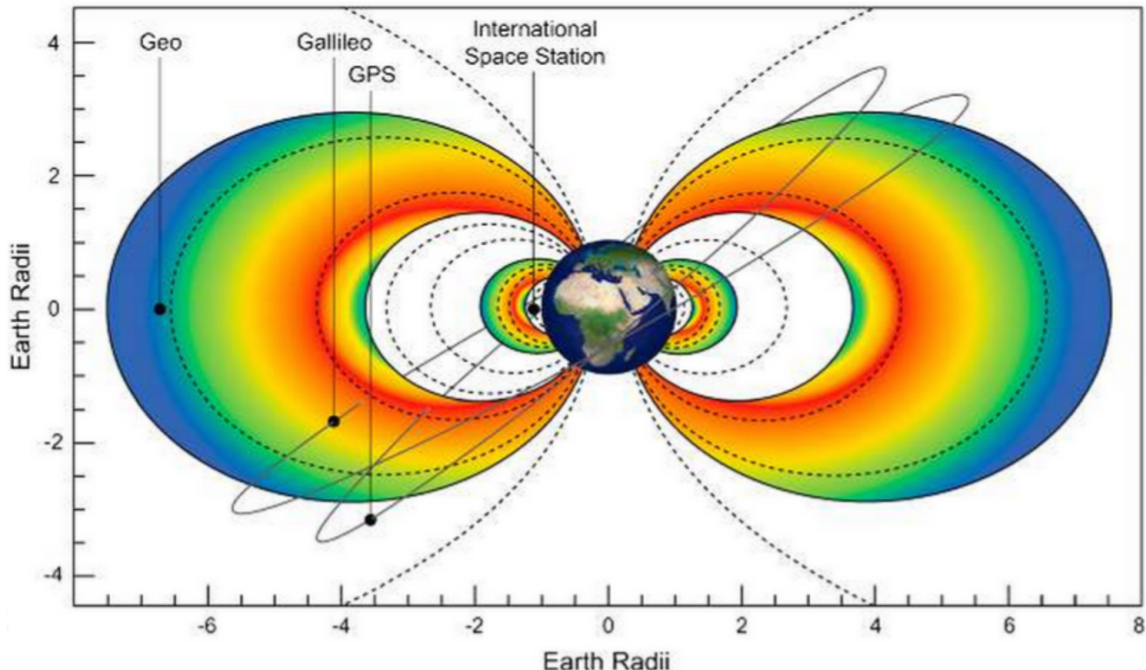


Figure 1.9: The two radiation belts with the locations of various satellites and orbits. Figure from (Horne et al., 2013).

¹⁸¹ Radiation Belts The highest energy particle populations are in the Van Allen
¹⁸² radiation belts. These belts were discovered by Van Allen (1959) and Vernov and
¹⁸³ Chudakov (1960) during the Cold War and are a pair of toroidally shaped populations
¹⁸⁴ of trapped electrons and protons usually within to $L < 8$ and are shown in Fig. 1.9.
¹⁸⁵ Their quiescent toroidal shape is similar to the shape of the plasmasphere and ring
¹⁸⁶ current and is a result of Earth's dipole magnetic field and the conservation of the
¹⁸⁷ three adiabatic invariants discussed in section 1.

¹⁸⁸ The inner radiation belt is extremely stable on time periods of years, extends
¹⁸⁹ to $L \approx 2$, and mainly consists of protons with energies between MeV and GeV and
¹⁹⁰ electrons with energies up to ≈ 1 MeV (Claudepierre et al., 2019). The source of
¹⁹¹ inner radiation belt protons is believed to be due to cosmic-ray albedo neutron decay

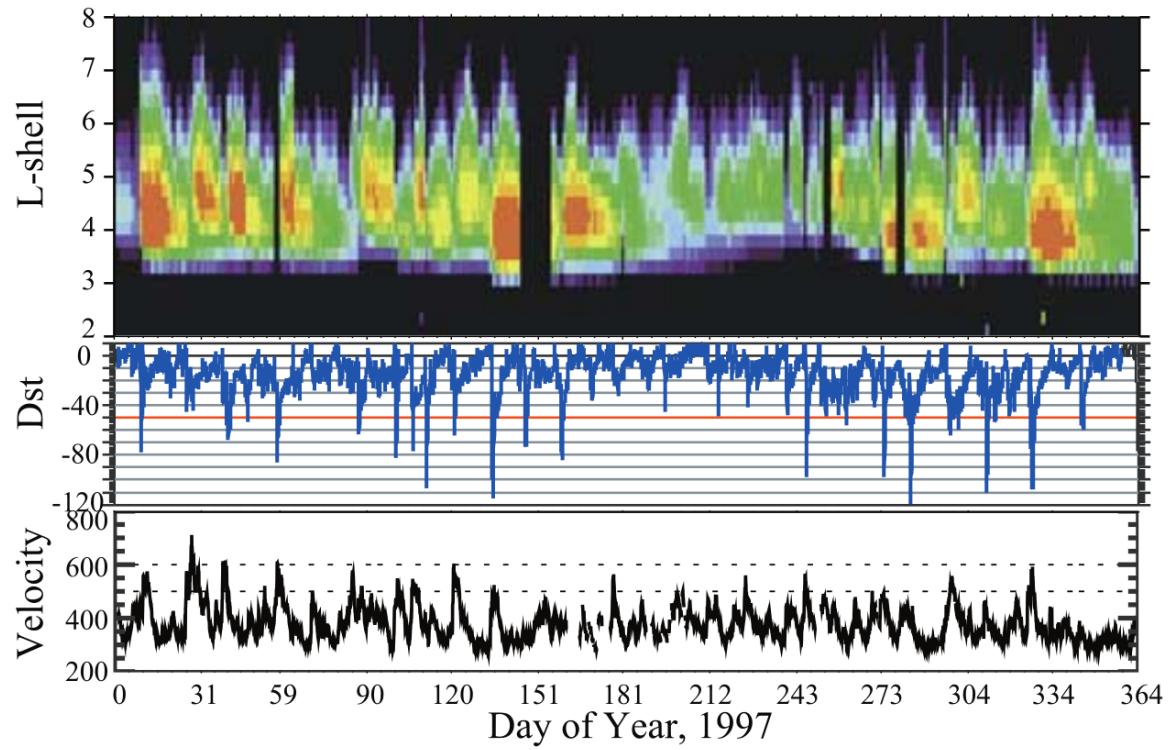


Figure 1.10: The dynamics of the outer radiation belt in 1997 from the POLAR satellite. Top panel shows the 1.2-2.4 MeV electron flux as a function of L and 1997 day of year. The middle panel shows the DST index, and bottom panel shows the solar wind velocity. Figure from (Reeves et al., 2003).

192 (e.g. Li et al., 2017) and inward radial diffusion for electrons (e.g. O'Brien et al.,
 193 2016). The gap between the inner and outer radiation belt is called the slot, which is
 194 believed to be due to hiss waves inside the plasmasphere (described below) scattering
 195 particles into the atmosphere (e.g. Breneman et al., 2015; Lyons and Thorne, 1973).

196 The outer radiation belt, on the other hand is much more dynamic and consists
 197 of mainly electrons of energies up to a few MeV. The outer belt's spatial extent is
 198 highly variable e.g. see Fig. 1.10, and is typically observed at $4 < L < 8$. Since
 199 the outer radiation belt contains a dynamic population of energetic particles that
 200 pose a threat to human and technological presence in Earth's atmosphere and space,
 201 decades of research has been undertaken to understand and predict the outer radiation
 202 belt particles, waves, and wave-particle interactions. The dynamics of the outer
 203 radiation belt can be understood by considering various competing acceleration and
 204 loss mechanisms which will be described in the following sections.

205

Radiation Belt Particle Sources and Sinks

206 Adiabatic Heating

207 One of the particle heating and transport mechanisms arises from the Earthward
 208 convection of particles. The conservation of J_1 implies that the initial and final v_\perp
 209 depends on the change in the magnetic field amplitude

$$\frac{v_{\perp i}^2}{B_i} = \frac{v_{\perp f}^2}{B_f}. \quad (1.12)$$

210 As a particle convects Earthward, $B_f > B_i$ thus v_\perp must increase. The dipole
 211 magnetic field amplitude can be written as

$$B(L, \theta) = \frac{31.2 \mu\text{T}}{L^3} \sqrt{1 + 3 \cos^2 \theta} \quad (1.13)$$

²¹² which implies that

$$\frac{v_{\perp f}^2}{v_{\perp i}^2} = \left(\frac{L_i}{L_f}\right)^3. \quad (1.14)$$

²¹³ .

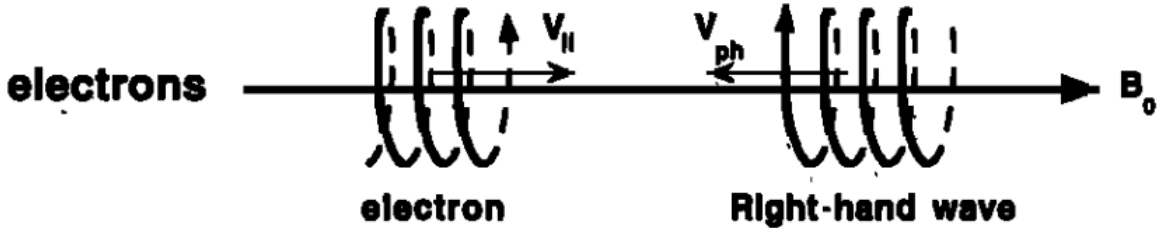
²¹⁴ In addition, as the particle convects Earthward the distance between the
²¹⁵ particle's mirror points decrease. If J_2 is conserved, the shrinking bounce path implies
²¹⁶ that $v_{||}$ must increase by

$$\frac{v_{|| f}^2}{v_{|| i}^2} = \left(\frac{L_i}{L_f}\right)^k \quad (1.15)$$

²¹⁷ where k ranges from 2 for equatorial pitch angles, $\alpha_{eq} = 0^\circ$, to 2.5 for $\alpha_{eq} = 90^\circ$
²¹⁸ (Baumjohann and Treumann, 1997). Since the rate of adiabatic heating is greater in
²¹⁹ the perpendicular direction than heating in the parallel direction, an initially isotropic
²²⁰ particle distribution will become anisotropic during its convection. These isotropic
²²¹ particles can then become unstable to wave growth and generate waves in order to
²²² reach equilibrium.

²²³ Wave Resonance Heating

²²⁴ Another mechanism that heats particles is due to particles resonating with
²²⁵ plasma waves. A few of the electromagnetic wave modes responsible for particle
²²⁶ acceleration (and deceleration) relevant to radiation belt dynamics are hiss, whistler
²²⁷ mode chorus (chorus), and electromagnetic ion cyclotron (EMIC) waves. These waves
²²⁸ are created by the loss cone instability that driven by an anisotropy of electrons
²²⁹ for chorus waves, and protons for EMIC waves. The level of anisotropy can be
²³⁰ quantified by the ratio of the perpendicular to parallel particle temperatures ($T_{\perp}/T_{||}$).
²³¹ A particle distribution is unstable when $T_{\perp}/T_{||} > 1$ which facilitates wave growth.



$$\omega + k_{\parallel} v_{\parallel} = \Omega^-$$

Figure 1.11: The trajectories of an electron and a right-hand circularly polarized wave during a cyclotron resonance. The electron's v_{\parallel} and the wave's k_{\parallel} are in opposite directions such that the wave's frequency is Doppler shifted to an integer multiple of the electron cyclotron frequency. Figure from (Tsurutani and Lakhina, 1997).

232 Since electrons gyrate in a right-handed sense, the chorus waves also tend to be right
 233 hand circularly polarized (Tsurutani and Lakhina, 1997). The same argument applies
 234 to protons and left hand circularly polarized EMIC waves as well.

235 These circularly polarized waves can resonate with electrons and/or protons
 236 when their combined motion results in a static \vec{E} . One example of a resonance
 237 between a right hand circularly polarized wave and an electron is shown in Fig. 1.21
 238 and is termed the cyclotron resonance. An electron's v_{\parallel} and the wave's parallel wave
 239 vector, k_{\parallel} are in opposite directions such that the wave frequency ω is Doppler shifted
 240 to an integer multiple of the Ω_e at which point the electron feels a static electric
 241 field and is accelerated or decelerated. This acceleration happens when a resonance
 242 condition is satisfied between a wave and a particle for which we will now derive an
 243 illustrative toy model.

244 Assume a uniform magnetic field $\vec{B} = B_0 \hat{z}$ with a parallel propagating ($k = k\hat{z}$),
 245 right-hand circularly polarized wave. The wave's electric field as a function of position
 246 and time can be written as

$$\vec{E} = E_0 (\cos(\omega t - kz) \hat{x} + \sin(\omega t - kz) \hat{y}) \quad (1.16)$$

which is more clearly expressed by taking the dot product to find \vec{E} in the $\hat{\theta}$ direction

$$E_\theta = \vec{E} \times \hat{\theta} = E_0 \cos(\omega t - kz + \theta). \quad (1.17)$$

²⁴⁷ Now assume that the electron is traveling in the $-\hat{z}$ direction with a velocity $\vec{v} = -v_0 \hat{z}$
²⁴⁸ so its time dependent position along \hat{z} is

$$z(t) = -v_0 t \quad (1.18)$$

²⁴⁹ and gyrophase is

$$\theta(t) = -\Omega t + \theta(0) \quad (1.19)$$

²⁵⁰ where the first negative sign comes from the electron's negative charge. Now we put
²⁵¹ this all together and express the electric field and the force that the electron will
²⁵² experience

$$m \frac{dv_\theta}{dt} = qE_\theta = qE_0 \sin((\omega + kv_0 - \Omega)t + \theta(0)). \quad (1.20)$$

²⁵³ This is a relatively complex expression, but when the time dependent component,

$$\omega + kv_0 - \Omega = 0, \quad (1.21)$$

²⁵⁴ the electron will be in a static electric field which will accelerate or decelerate the
²⁵⁵ electron depending on θ_0 , the phase between the wave and the electron. **Show Bortnik
²⁵⁶ 2008 plot?** The expression in Eq. 1.21 is commonly referred to as the resonance

²⁵⁷ condition and is more generally written as

$$\omega - k_{||}v_{||} = \frac{n\Omega_e}{\gamma} \quad (1.22)$$

²⁵⁸ where n is the resonance order, and γ is the relativistic correction (e.g. Millan
²⁵⁹ and Thorne, 2007). It is important to remember that along the particle's orbit it
²⁶⁰ will encounter and experience the effects of all of the waves along its orbit. The
²⁶¹ typical MLT extent of a handful of waves that are capable of scattering radiation belt
²⁶² electrons are shown in Fig. 1.12.

²⁶³ Particle Losses

²⁶⁴ There are various transport or scatter mechanisms that result in the loss of
²⁶⁵ radiation belt particles into the atmosphere or the solar wind. One of the loss
²⁶⁶ mechanisms of particles into the solar wind is magnetopause shadowing (Ukhorskiy
²⁶⁷ et al., 2006). Recall that when the ring current is strengthened, the magnetic field is
²⁶⁸ reduced on Earth's surface and increased outside of the ring current. If the time scale
²⁶⁹ of the ring current strengthening is slower than a particle drift, the third adiabatic
²⁷⁰ invariant is conserved. In order to conserve the third adiabatic invariant while the
²⁷¹ magnetic field strength is increasing outside of the ring current, the particle's orbit
²⁷² gradually moves outward. If the particle drift shell crosses the magnetopause the
²⁷³ particle will then be lost to the solar wind.

²⁷⁴ **Move to acceleration?** Another particle loss (and acceleration) mechanism is
²⁷⁵ driven by ultra low frequency (ULF) waves and is called radial diffusion. Radial
²⁷⁶ diffusion is the transport of particles from high to low phase space density, f . If
²⁷⁷ the transport is radially inward, particles will appear to be accelerated. On the
²⁷⁸ other hand, radially outward radial diffusion can transport particles through the
²⁷⁹ magnetopause where they will be lost. Reeves et al. (2013) investigated the driver of

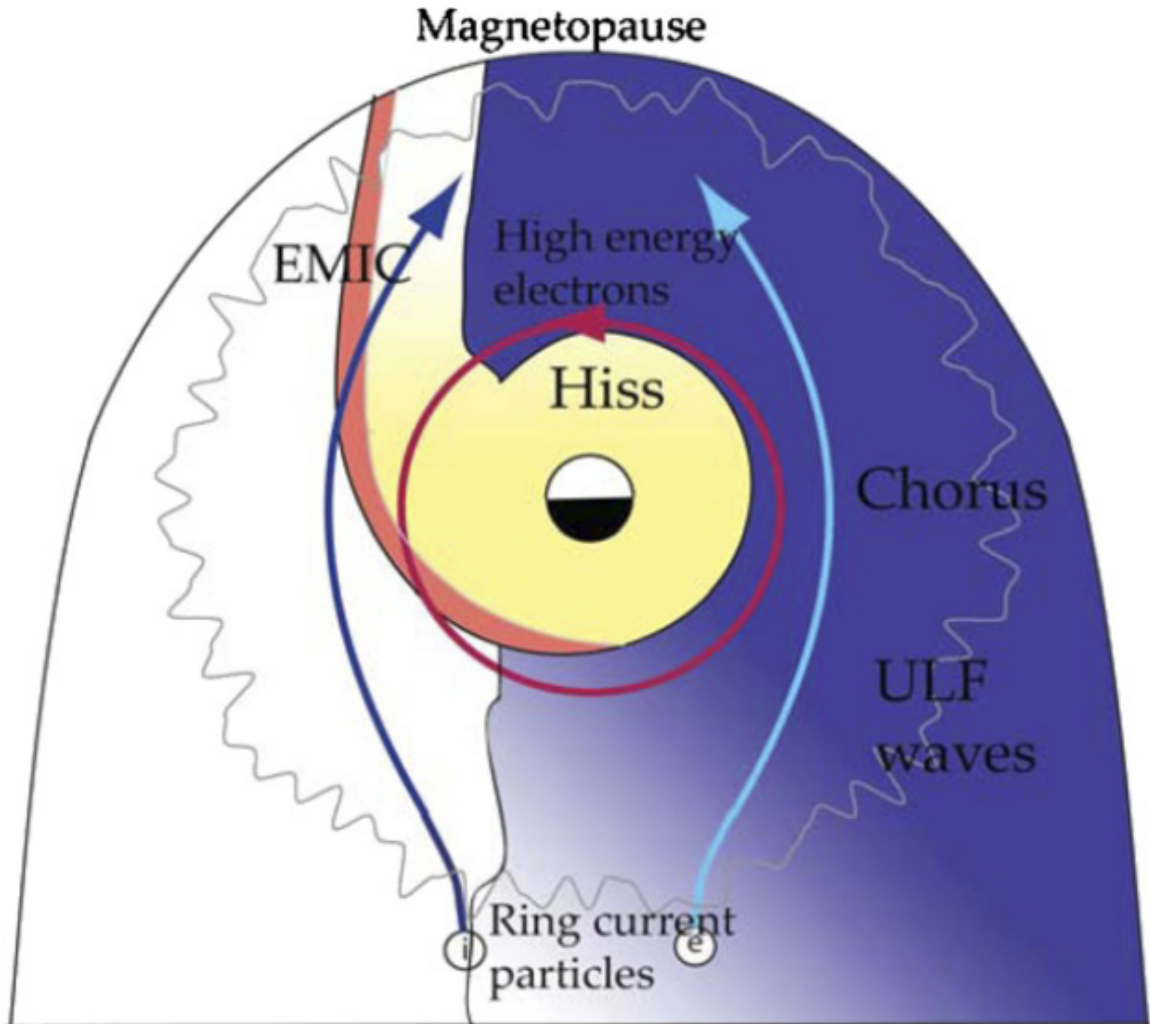


Figure 1.12: Various wave modes in the magnetosphere. Ultra low frequency waves occur through the magnetosphere. Chorus waves are typically observed in the 0-12 midnight-dawn region. EMIC waves are typically observed in the dusk MLT sector. Hiss waves are observed inside the plasmasphere. Figure from Millan and Thorne (2007).

280 particle acceleration during the October 2012 storm and observationally found that
 281 inward radial diffusion was not dominant, rather local acceleration via pitch angle
 282 diffusion which will be described below appeared to be the dominant acceleration
 283 mechanism.

284 The loss mechanism central to this dissertation is pitch angle and energy
 285 scattering of electrons by waves such as plasmaspheric hiss (e.g. Breneman et al.,
 286 2015), EMIC waves (e.g. Capannolo et al., 2019), and chorus waves (e.g. Breneman
 287 et al., 2017). These wave-particle interactions occur when the resonance condition
 288 in Eq. 1.21 is satisfied. When it is satisfied the particle's energy and α is modified
 289 by the wave. If the wave changes α towards 0 such that $\alpha < \alpha_{LC}$, the particle's
 290 mirror point lowers below ≈ 100 km altitude and can be lost due collisions with air.
 291 Some of these electrons can be impulsively scattered into the loss cone where they
 292 are observed as a sub second duration enhancements termed microbursts.

293

Microbursts

294 Anderson and Milton (1964) first reported microbursts from high altitude
 295 balloon observations of bremsstrahlung X-rays emitted by microburst electrons
 296 impacting the atmosphere. Over the decades since then, microbursts have been
 297 observed on many other balloon missions (e.g. Anderson et al., 2017; Parks, 1967;
 298 Woodger et al., 2015). In addition to the X-ray signature, microbursts electrons
 299 have been directly observed in LEO with LEO spacecraft including the Solar
 300 Anomalous and Magnetospheric Particle Explorer (SAMPEX), Focused Investigation
 301 of Relativistic Electron Bursts: Intensity, Range, and Dynamics II (FIREBIRD-II),
 302 Science Technologies Satellite (STSAT-I) (e.g. Blake et al., 1996; Blum et al., 2015;
 303 Breneman et al., 2017; Crew et al., 2016; Lee et al., 2012, 2005; Lorentzen et al.,
 304 2001a,b; Nakamura et al., 1995, 2000; O'Brien et al., 2004, 2003). An example

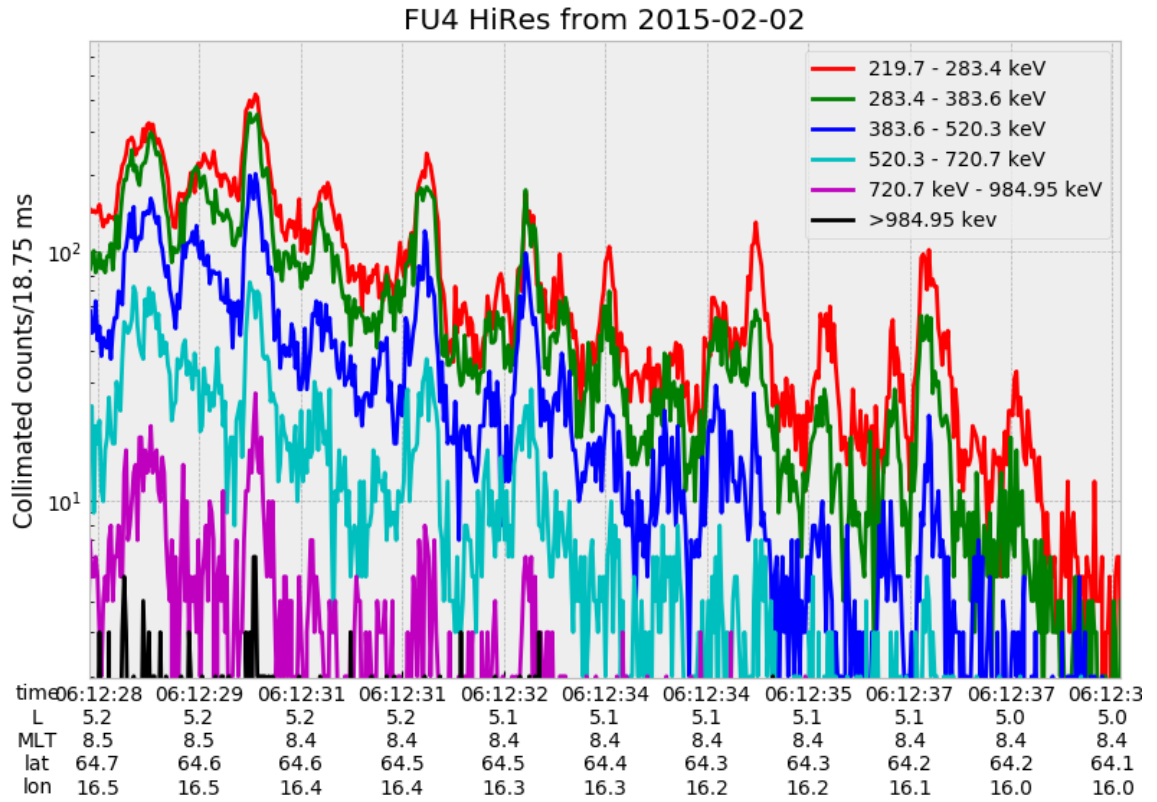


Figure 1.13: An example train of microbursts observed by FIREBIRD-II unit 4 on February 2nd, 2015. The colored curves show the differential energy channel count rates in six channels from ≈ 200 keV to greater than 1 MeV. The x-axis labels show auxiliary information such as time of observation and the spacecraft position in L, MLT, latitude and longitude coordinates.

305 microburst time series is shown in Fig. 1.13.

306 Microbursts are observed on magnetic field footprints that are connected to
 307 the outer radiation belt, and are predominately observed in the 0-12 MLT sector
 308 with an elevated occurrence frequency during disturbed times as shown in Fig. 1.14.
 309 Microbursts have been observed over a wide energy range from a few tens of keV
 310 (Datta et al., 1997) to greater than 1 MeV (e.g. Blake et al., 1996; Greeley et al.,
 311 2019). The microburst electron flux (J) vs energy spectra is typically well fit to a

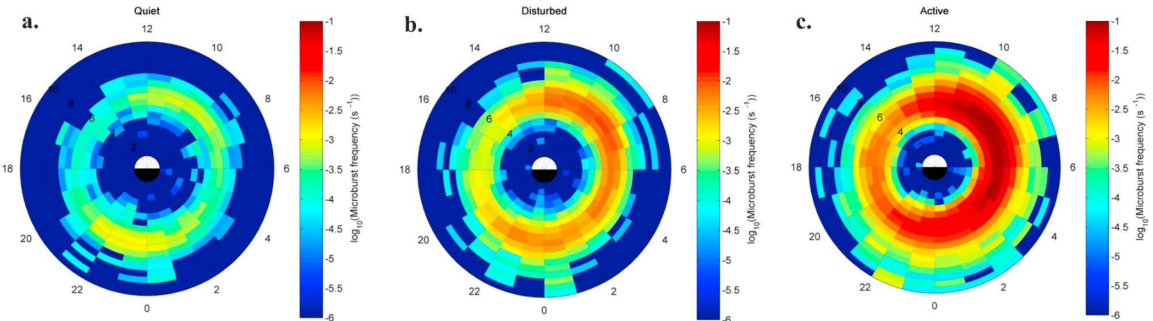


Figure 1.14: Relativistic ($> 1\text{MeV}$) distribution of microburst occurrence rates as a function of L and MLT. The three panels explore the microburst occurrence rate dependence on geomagnetic activity parameterized by the auroral electrojet index for (a) $\text{AE} < 100 \text{nT}$, (b) $100 < \text{AE} < 300 \text{nT}$ and (c) $\text{AE} > 300 \text{nT}$. Figure from Douma et al. (2017).

312 decaying exponential (e.g. (Lee et al., 2005; Parks, 1967))

$$J(E) = J_0 e^{-E/E_0} \quad (1.23)$$

313 where J_0 is the flux at 0 keV (unphysical free parameter) and E_0 quantifies the
 314 efficiency of the scattering mechanism in energy. A small E_0 suggests that mostly high
 315 energy particles are scattered and a high E_0 suggests that the scattering mechanism
 316 scatters low and high energy electrons. In reality, a high E_0 may be a signature of a
 317 high energy electron scattering mechanism, but is hidden by the convolution of the
 318 source particles available to be scattered (typically with a falling energy spectrum)
 319 and the energy-dependent scattering efficiency.

320 The short microburst duration observed by a single LEO satellite creates an
 321 ambiguity in interpreting what is exactly a microbursts. Is a microburst very small
 322 and spatially stationary so that the LEO spacecraft flies through it in less than a
 323 second, or are microbursts large, but short duration such that the microburst comes
 324 and goes in a fraction of a second? A high altitude balloon provides essentially a

325 stationary view of the radiation belt footprints and a temporal microburst can be
 326 unambiguously identified, but a spatial structure is very difficult to identify.

327 Multi-spacecraft missions are better equipped to determine if a microburst is
 328 spatial or temporal. As will be shown in this dissertation, if a microburst is observed
 329 simultaneously by two spacecraft then it is temporally transient with a size greater
 330 than the spacecraft separation. On the other hand, if two spacecraft observe a
 331 microburst-like feature in the same location and at different times, then it is spatial
 332 and called a curtain (Blake and O'Brien, 2016).

333 the microburst size and if it is spatial or temporal, and a balloon can easily
 334 observe the temporal microbursts but have limited spatial information. Both
 335 observation methods have a unique set of strengths and weaknesses, and this
 336 dissertation takes the multi-spacecraft approach to analyze the size of microbursts.

337

Scope of Research

338 This dissertation furthers our understanding of the microburst scattering
 339 mechanism and is organized into the following chapters. Chapter X will describe
 340 the spacecraft missions used to study microburst precipitation and wave-particle
 341 scattering. Then Ch. Y will describe a microburst scattering event observed by
 342 NASA's Van Allen Probes and the quasi-linear diffusion model that was developed.
 343 Next, Ch. Z will describe a bouncing packet microburst observation made by
 344 MSU's FIREBIRD-II mission where the microburst's lower bound longitudinal and
 345 latitudinal scale sizes were estimated. Chapter ZZ then expands the case study result
 346 from Ch. Z to a statistical study of microburst sizes and the microburst size models
 347 developed to interpret the data. Lastly, ZZZ will summarize the dissertation work
 348 and make concluding remarks about research to be done.

349 **Mention a theme for the three papers.**

- 351 Anderson, B., Shekhar, S., Millan, R., Crew, A., Spence, H., Klumpar, D., Blake, J.,
 352 O'Brien, T., and Turner, D. (2017). Spatial scale and duration of one microburst
 353 region on 13 August 2015. *Journal of Geophysical Research: Space Physics*.
- 354 Anderson, K. A. and Milton, D. W. (1964). Balloon observations of X rays in the
 355 auroral zone: 3. High time resolution studies. *Journal of Geophysical Research*,
 356 69(21):4457–4479.
- 357 Baumjohann, W. and Treumann, R. A. (1997). *Basic space plasma physics*. World
 358 Scientific.
- 359 Blake, J.,Looper, M., Baker, D., Nakamura, R., Klecker, B., and Hovestadt, D.
 360 (1996). New high temporal and spatial resolution measurements by sampex of the
 361 precipitation of relativistic electrons. *Advances in Space Research*, 18(8):171 – 186.
- 362 Blake, J. B. and O'Brien, T. P. (2016). Observations of small-scale latitudinal
 363 structure in energetic electron precipitation. *Journal of Geophysical Research: Space Physics*, 121(4):3031–3035. 2015JA021815.
- 365 Blum, L., Li, X., and Denton, M. (2015). Rapid MeV electron precipitation as
 366 observed by SAMPEX/HILT during high-speed stream-driven storms. *Journal of
 367 Geophysical Research: Space Physics*, 120(5):3783–3794. 2014JA020633.
- 368 Breneman, A., Crew, A., Sample, J., Klumpar, D., Johnson, A., Agapitov, O.,
 369 Shumko, M., Turner, D., Santolik, O., Wygant, J., et al. (2017). Observations
 370 directly linking relativistic electron microbursts to whistler mode chorus: Van allen
 371 probes and FIREBIRD II. *Geophysical Research Letters*.
- 372 Breneman, A. W., Halford, A., Millan, R., McCarthy, M., Fennell, J., Sample, J.,
 373 Woodger, L., Hospodarsky, G., Wygant, J. R., Cattell, C. A., et al. (2015). Global-
 374 scale coherence modulation of radiation-belt electron loss from plasmaspheric hiss.
 375 *Nature*, 523(7559):193.
- 376 Capannolo, L., Li, W., Ma, Q., Shen, X.-C., Zhang, X.-J., Redmon, R., Rodriguez,
 377 J., Engebretson, M., Kletzing, C., Kurth, W., et al. (2019). Energetic electron
 378 precipitation: multi-event analysis of its spatial extent during emic wave activity.
 379 *Journal of Geophysical Research: Space Physics*.
- 380 Claudepierre, S., O'Brien, T.,Looper, M., Blake, J., Fennell, J., Roeder, J.,
 381 Clemmons, J., Mazur, J., Turner, D., Reeves, G., et al. (2019). A revised look
 382 at relativistic electrons in the earth's inner radiation zone and slot region. *Journal
 383 of Geophysical Research: Space Physics*, 124(2):934–951.

- 384 Crew, A. B., Spence, H. E., Blake, J. B., Klumpar, D. M., Larsen, B. A., O'Brien,
 385 T. P., Driscoll, S., Handley, M., Legere, J., Longworth, S., Mashburn, K.,
 386 Mosleh, E., Ryhajlo, N., Smith, S., Springer, L., and Widholm, M. (2016). First
 387 multipoint in situ observations of electron microbursts: Initial results from the
 388 NSF FIREBIRD II mission. *Journal of Geophysical Research: Space Physics*,
 389 121(6):5272–5283. 2016JA022485.
- 390 Datta, S., Skoug, R., McCarthy, M., and Parks, G. (1997). Modeling of microburst
 391 electron precipitation using pitch angle diffusion theory. *Journal of Geophysical
 392 Research: Space Physics*, 102(A8):17325–17333.
- 393 Douma, E., Rodger, C. J., Blum, L. W., and Clilverd, M. A. (2017). Occurrence
 394 characteristics of relativistic electron microbursts from SAMPEX observations.
 395 *Journal of Geophysical Research: Space Physics*, 122(8):8096–8107. 2017JA024067.
- 396 Dungey, J. W. (1961). Interplanetary magnetic field and the auroral zones. *Phys.
 397 Rev. Lett.*, 6:47–48.
- 398 Greeley, A., Kanekal, S., Baker, D., Klecker, B., and Schiller, Q. (2019). Quantifying
 399 the contribution of microbursts to global electron loss in the radiation belts. *Journal
 400 of Geophysical Research: Space Physics*.
- 401 Horne, R., Glauert, S., Meredith, N., Boscher, D., Maget, V., Heynderickx, D., and
 402 Pitchford, D. (2013). Space weather impacts on satellites and forecasting the earth's
 403 electron radiation belts with spacecast. *Space Weather*, 11(4):169–186.
- 404 Horne, R. B., Thorne, R. M., Shprits, Y. Y., Meredith, N. P., Glauert, S. A., Smith,
 405 A. J., Kanekal, S. G., Baker, D. N., Engebretson, M. J., Posch, J. L., et al.
 406 (2005). Wave acceleration of electrons in the van allen radiation belts. *Nature*,
 407 437(7056):227.
- 408 Lee, J. J., Parks, G. K., Lee, E., Tsurutani, B. T., Hwang, J., Cho, K. S., Kim, K.-H.,
 409 Park, Y. D., Min, K. W., and McCarthy, M. P. (2012). Anisotropic pitch angle
 410 distribution of 100 keV microburst electrons in the loss cone: measurements from
 411 STSAT-1. *Annales Geophysicae*, 30(11):1567–1573.
- 412 Lee, J.-J., Parks, G. K., Min, K. W., Kim, H. J., Park, J., Hwang, J., McCarthy,
 413 M. P., Lee, E., Ryu, K. S., Lim, J. T., Sim, E. S., Lee, H. W., Kang, K. I., and
 414 Park, H. Y. (2005). Energy spectra of 170–360 keV electron microbursts measured
 415 by the korean STSAT-1. *Geophysical Research Letters*, 32(13). L13106.
- 416 Li, X., Selesnick, R., Schiller, Q., Zhang, K., Zhao, H., Baker, D. N., and Temerin,
 417 M. A. (2017). Measurement of electrons from albedo neutron decay and neutron
 418 density in near-earth space. *Nature*, 552(7685):382.

- 419 Lorentzen, K. R., Blake, J. B., Inan, U. S., and Bortnik, J. (2001a). Observations
 420 of relativistic electron microbursts in association with VLF chorus. *Journal of*
 421 *Geophysical Research: Space Physics*, 106(A4):6017–6027.
- 422 Lorentzen, K. R.,Looper, M. D., and Blake, J. B. (2001b). Relativistic electron
 423 microbursts during the GEM storms. *Geophysical Research Letters*, 28(13):2573–
 424 2576.
- 425 Lyons, L. R. and Thorne, R. M. (1973). Equilibrium structure of radiation belt
 426 electrons. *Journal of Geophysical Research*, 78(13):2142–2149.
- 427 Millan, R. and Thorne, R. (2007). Review of radiation belt relativistic electron losses.
 428 *Journal of Atmospheric and Solar-Terrestrial Physics*, 69(3):362 – 377.
- 429 Nakamura, R., Baker, D. N., Blake, J. B., Kanekal, S., Klecker, B., and Hovestadt,
 430 D. (1995). Relativistic electron precipitation enhancements near the outer edge of
 431 the radiation belt. *Geophysical Research Letters*, 22(9):1129–1132.
- 432 Nakamura, R., Isowa, M., Kamide, Y., Baker, D., Blake, J., and Looper, M. (2000).
 433 Observations of relativistic electron microbursts in association with VLF chorus.
 434 *J. Geophys. Res.*, 105:15875–15885.
- 435 O'Brien, T., Claudepierre, S., Guild, T., Fennell, J., Turner, D., Blake, J., Clemmons,
 436 J., and Roeder, J. (2016). Inner zone and slot electron radial diffusion revisited.
 437 *Geophysical Research Letters*, 43(14):7301–7310.
- 438 O'Brien, T. and Moldwin, M. (2003). Empirical plasmapause models from magnetic
 439 indices. *Geophysical Research Letters*, 30(4).
- 440 O'Brien, T. P., Looper, M. D., and Blake, J. B. (2004). Quantification of relativistic
 441 electron microburst losses during the GEM storms. *Geophysical Research Letters*,
 442 31(4). L04802.
- 443 O'Brien, T. P., Lorentzen, K. R., Mann, I. R., Meredith, N. P., Blake, J. B., Fennell,
 444 J. F., Looper, M. D., Milling, D. K., and Anderson, R. R. (2003). Energization of
 445 relativistic electrons in the presence of ULF power and MeV microbursts: Evidence
 446 for dual ULF and VLF acceleration. *Journal of Geophysical Research: Space*
 447 *Physics*, 108(A8).
- 448 Parks, G. K. (1967). Spatial characteristics of auroral-zone X-ray microbursts. *Journal*
 449 *of Geophysical Research*, 72(1):215–226.
- 450 Reeves, G., Spence, H. E., Henderson, M., Morley, S., Friedel, R., Funsten, H., Baker,
 451 D., Kanekal, S., Blake, J., Fennell, J., et al. (2013). Electron acceleration in the
 452 heart of the van allen radiation belts. *Science*, 341(6149):991–994.

- 453 Reeves, G. D., McAdams, K. L., Friedel, R. H. W., and O'Brien, T. P. (2003). Acceleration and loss of relativistic electrons during geomagnetic storms. *Geophysical Research Letters*, 30(10):n/a–n/a. 1529.
- 456 Schulz, M. and Lanzerotti, L. J. (1974). *Particle Diffusion in the Radiation Belts*. Springer.
- 458 Tsurutani, B. T. and Lakhina, G. S. (1997). Some basic concepts of wave-particle interactions in collisionless plasmas. *Reviews of Geophysics*, 35(4):491–501.
- 460 Turner, D., Claudepierre, S., Fennell, J., O'Brien, T., Blake, J., Lemon, C., Gkioulidou, M., Takahashi, K., Reeves, G., Thaller, S., et al. (2015). Energetic electron injections deep into the inner magnetosphere associated with substorm activity. *Geophysical Research Letters*, 42(7):2079–2087.
- 464 Ukhorskiy, A. Y., Anderson, B. J., Brandt, P. C., and Tsyganenko, N. A. (2006). Storm time evolution of the outer radiation belt: Transport and losses. *Journal of Geophysical Research: Space Physics*, 111(A11):n/a–n/a. A11S03.
- 467 Van Allen, J. A. (1959). The geomagnetically trapped corpuscular radiation. *Journal of Geophysical Research*, 64(11):1683–1689.
- 469 Vernov, S. and Chudakov, A. (1960). Investigation of radiation in outer space. In *International Cosmic Ray Conference*, volume 3, page 19.
- 471 Woodger, L., Halford, A., Millan, R., McCarthy, M., Smith, D., Bowers, G., Sample, J., Anderson, B., and Liang, X. (2015). A summary of the BARREL campaigns: Technique for studying electron precipitation. *Journal of Geophysical Research: Space Physics*, 120(6):4922–4935.